ARTICLES
https://doi.org/10.1038/s41565-019-0486-y
nature nanotechnology

Theoretical strength and rubber-like behaviour in micro-sized pyrolytic carbon

Xuan Zhang[1,4], Lei Zhong[1,4], Arturo Mateos[2,4], Akira Kudo[2], Andrey Vyatskikh[2], Huajian Gao[3*], Julia R. Greer[2*] and Xiaoyan Li[1*]

The creation of materials with a combination of high strength, substantial deformability and ductility, large elastic limit and low density represents a long-standing challenge, because these properties are, in general, mutually exclusive. Using a combination of two-photon lithography and high-temperature pyrolysis, we have created micro-sized pyrolytic carbon with a tensile strength of 1.60 ± 0.55 GPa, a compressive strength approaching the theoretical limit of ~13.7 GPa, a substantial elastic limit of 20–30% and a low density of ~1.4 g cm^{-3}. This corresponds to a specific compressive strength of 9.79 GPa cm^3 g^{-1}, a value that surpasses that of nearly all existing structural materials. Pillars with diameters below 2.3 μm exhibit rubber-like behaviour and sustain a compressive strain of ~50% without catastrophic failure; larger ones exhibit brittle fracture at a strain of ~20%. Large-scale atomistic simulations reveal that this combination of beneficial mechanical properties is enabled by the local deformation of 1 nm curled graphene fragments within the pyrolytic carbon microstructure, the interactions among neighbouring fragments and the presence of covalent carbon–carbon bonds.

In modern advanced material design, the creation of high-performance materials that combine high strength, substantial deformability, large elastic limit, and low density is a long-standing goal and challenge. Two pairs of apparent conflicts exist for nearly all structural materials that include metals/alloys[1], polymers[2] and porous materials like foams[3], nanolattices[4] and nanosponges[5]: high strength versus high deformability/ductility and high strength versus low density. Tailoring the microstructures[6–8] or intrinsic/extrinsic dimensions[9–11] is an effective way to alter the mechanical properties of materials and to overcome these conflicts.

Two well-known carbon allotropes[12], graphene and carbon nanotubes, have 100% sp^2 bonds and ultra-high tensile strengths of ~100 GPa (ref. [13]), but their mechanical properties are sensitive to defects like vacancies, dislocations and grain boundaries[14–17]. The small dimensions of individual graphene sheets and nanotubes render them impractical for structural applications at large scales; their three-dimensional (3D) assemblies exhibit superelastic behaviour via buckling and bending of basic building blocks and can be scaled up to the macroscopic level[18–21]. These porous 3D graphene assemblies have densities as low as 0.001–1.0 g cm^{-3} and superior elastic limits up to 50%, but they are weak, with strengths as low as 10 MPa (refs. [18–20]). Various pyrolytic carbon (PyC) materials have been synthesized via pyrolysis of polymeric precursors at 400–2,500 °C (refs. [22–26]). These PyC samples[23–25], with dimensions exceeding 100 μm, exhibited a compressive strength or hardness of >1 GPa at a density of 1.1–2.5 g cm^{-3} and usually fractured below 3% strain[25]. Glassy carbon nanolattices fabricated via 3D printing and pyrolysis[26,27] with strut diameters of ~200 nm and low densities of 0.3–0.7 g cm^{-3} achieved a compressive strength of ~300 MPa at a fracture strain below 10%. These studies highlight both the promise and challenges associated with the design and fabrication of high-performance materials that possess a combination of high strength, substantial ductility, large elastic limit and low density.

We created PyC micropillars with diameters of 0.7–12.7 μm using two-photon lithography and pyrolysis. In situ nanomechanical experiments revealed that the PyC micropillars have ultra-large elastic limits of 20–30%, high tensile and compressive strengths of 1.6 and 13.7 GPa, low densities of 1.4 g cm^{-3} and ultra-high specific strengths up to 9.79 GPa cm^3 g^{-1}.

Fabrication and structural characterization

Figure 1a presents a schematic of the fabrication process for cylindrical micropillars with diameters D in the range of 6–50 μm and heights of 12–100 μm, printed using two-photon lithography direct laser writing (TPL DLW) from a commercial IP-Dip photoresist. During fabrication via TPL DLW, the sample geometry and dimension can be accurately controlled. Subsequent pyrolysis at 900 °C for 5 h in vacuum leads to complete carbonization and 98% volume shrinkage of polymeric samples[27]. The resulting PyC pillars have diameters D ranging from 1.28 to 12.7 μm (Fig. 1b,c). A residual carbon ring visible on the silicon substrate reflects the footprint of the original pillar and the constraint posed by the substrate during pyrolysis. Some samples were fabricated with caps to accommodate the grips for uniaxial tension experiments. More synthesis details are provided in the Methods. We employed secondary ion mass spectrometry (SIMS) and elemental analysers to obtain elemental compositions of the PyC micropillars (see Methods), using commercial glassy carbon as reference. SIMS spectra reveal that the elemental compositions in PyC micropillars are virtually equivalent to those in commercial glassy carbon (see Methods).

Figure 1d presents a representative high-resolution transmission electron microscopy (HRTEM) image of a PyC pillar, with the selected area electron diffraction pattern in the inset, revealing its amorphous microstructure. The magnified transmission electron microscopy (TEM) images in Fig. 1e,f indicate the presence of numerous 1.0–1.5 nm curled atomic fragments, which create

[1]Centre for Advanced Mechanics and Materials, Applied Mechanics Laboratory, Department of Engineering Mechanics, Tsinghua University, Beijing, China. [2]Division of Engineering and Applied Science, California Institute of Technology, Pasadena, CA, USA. [3]School of Engineering, Brown University, Providence, RI, USA. [4]These authors contributed equally: Xuan Zhang, Lei Zhong, Arturo Mateos. *e-mail: Huajian_Gao@brown.edu; jrgreer@caltech.edu; xiaoyanlithu@tsinghua.edu.cn

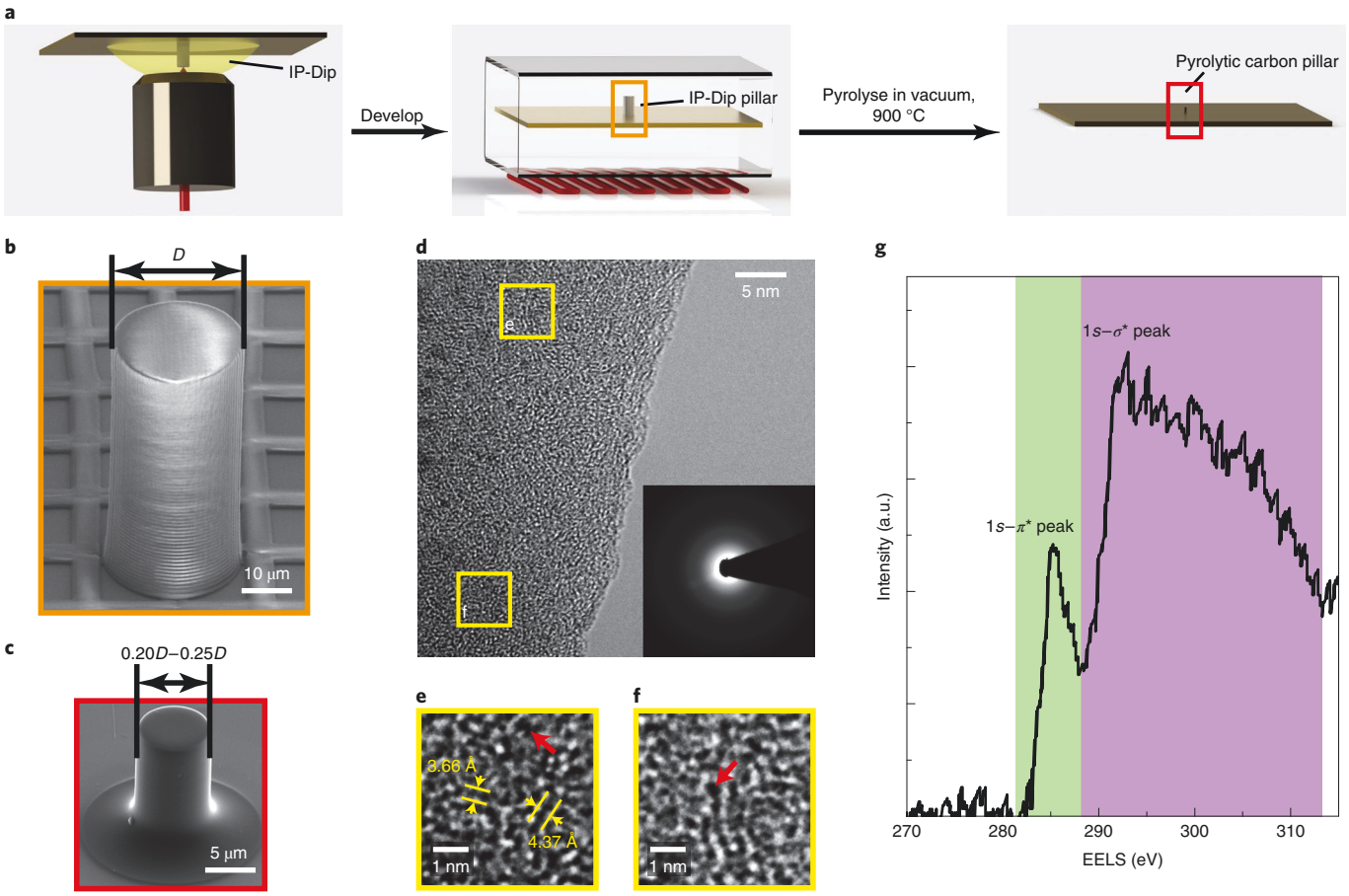

Fig. 1 | Fabrication and microstructural characterization of PyC micropillars. a, Schematic illustration of the fabrication process. This process includes TPL DLW of cylindrical pillars from IP-Dip polymer resin and subsequent pyrolysis under vacuum at 900 °C. **b**,**c**, Scanning electron microscopy (SEM) images of a representative micropillar before (**b**) and after (**c**) pyrolysis, showing substantial volumetric shrinkage. **d**, Bright-field TEM image of the PyC. The diffraction pattern in the inset reveals its amorphous microstructure. **e**,**f**, HRTEM images of the two regions outlined by solid boxes in **d**. These images reveal the presence of sub-nanometre-sized voids (denoted by red arrows). **g**, Typical EELS of the PyC, where the green and purple shaded areas correspond to the 1s-π^* and 1s-σ^* peaks of carbon, respectively.

sub-nanometre-sized voids distributed randomly throughout the pillar volume. Supplementary Figs. 1 and 2 show more HRTEM images of sections extracted from micropillars with different diameters prepared using low-energy focused ion beam (FIB) milling, revealing nearly the same microstructures as in Fig. 1d–f. The crystallite size (1.0–1.5 nm) of carbon layer fragments in our PyC samples is significantly smaller than those (~4–6 nm) of previously fabricated glassy carbon[23,25], with a similar interlayer spacing of ~0.31–0.39 nm. These microstructural features provide a useful foundation for estimating the density of PyC micropillars. Using a geometrical model[23], the experimentally measured density of 3D printed and subsequently pyrolysed resins, and atomistic modelling of PyC nanopillars, we determined the density of the PyC micropillars to be 1.4 g cm^{-3} (Supplementary Fig. 3 and Methods), which is close to that of low-density type-I glassy carbon[25,28]. Supplementary Fig. 4 shows the Raman spectra of PyC micropillars with D = 1.0–12.7 μm. By analysing these Raman spectra[29], we evaluated the average crystallite size within the carbon layer to be 1.7–2.5 nm (see Methods and Supplementary Table 1), which is consistent with the 1.0–1.5 nm determined from HRTEM observations. The typical electron energy loss spectroscopy (EELS) graph in Fig. 1g contains a 1s–σ^* peak at 292 eV and a 1s–π^* peak at 285 eV, which are consistent with the σ and π bonds characteristic of sp^2-hybridized carbon. Supplementary Fig. 5 shows all the EELS spectra measured at different sites of two micropillars with D = 2.3 and 12.7 μm; these display nearly identical trends and features. This suggests that PyC micropillars with different diameters have the same uniform microstructure and similar bonding structures. Using the two-window method[30], we estimated the fraction of sp^2 bonds calculated from EELS spectra (Fig. 1g and Supplementary Fig. 5) as 94.4 ± 3.2%, which indicates the dominance of sp^2 hybridization in PyC micropillars. The above microstructural characterization revealed that our PyC micropillar is an assembly of nanometre-sized curled graphene fragments interspersed with sub-nanometre-sized voids.

Nanomechanical experiments

Figure 2a shows all ex situ uniaxial compressive stress–strain data for micropillars with D = 4.6–12.7 μm. It appears that all micropillars deformed smoothly until failure, first deforming elastically up to ~20–30% strain, then yielding and plastically deforming over an additional ~8–10% strain before fracture. Nonlinear behaviours occurred during the first ~1–3% strain due to slight misalignment between the indenter tip and micropillar tops. We estimated the Young's modulus to be 16–26 GPa based on fitting the linear elastic portions of the stress–strain data in Fig. 2a. The failure strength of these micropillars increased from 3.8 GPa to 5.6 GPa with decreasing diameter. Figure 2b shows SEM images of a typical micropillar with D = 7.17 μm before and after deformation, suggesting that

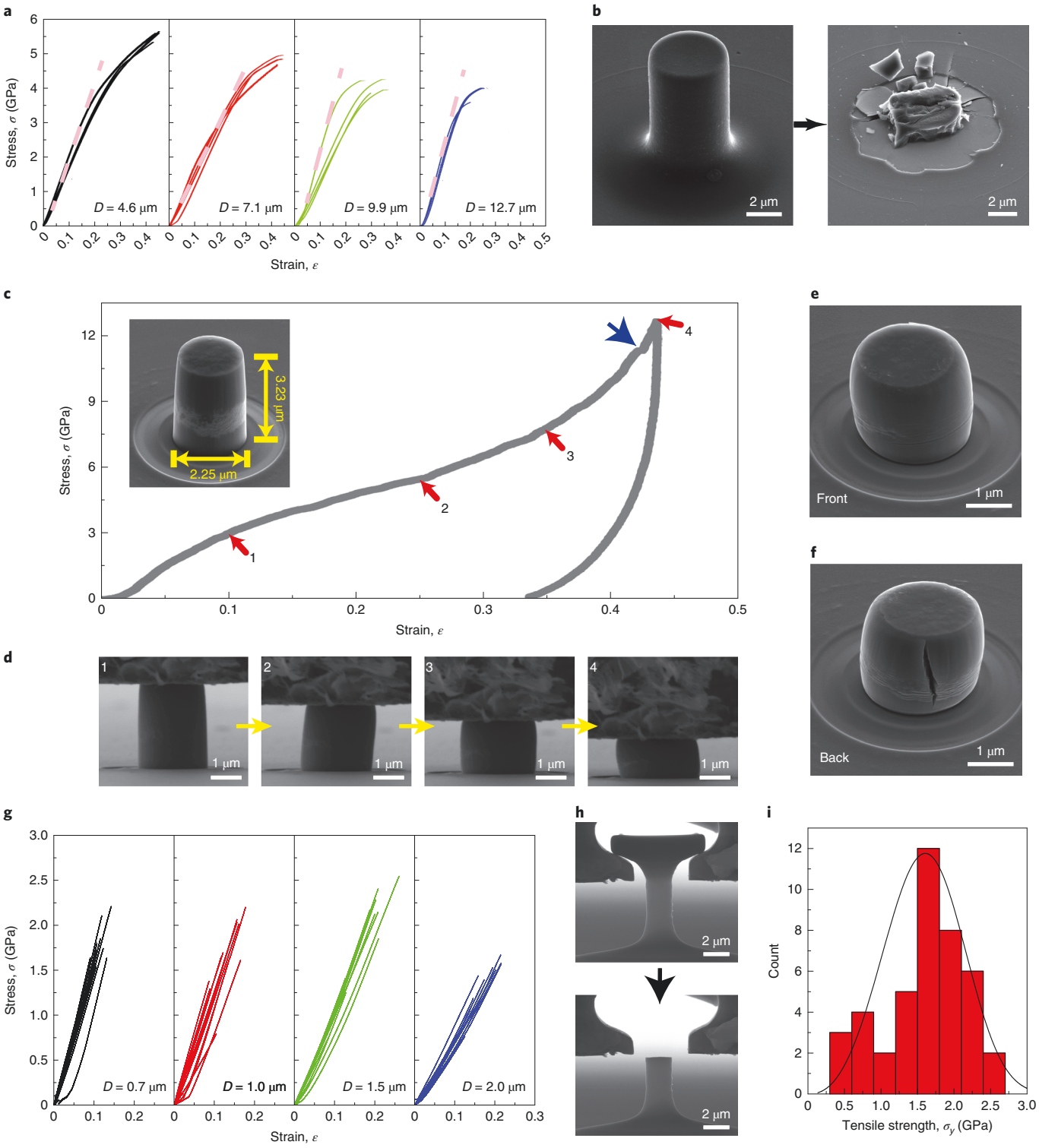

Fig. 2 | Uniaxial compression and tension experiments on PyC micropillars. a, Compressive stress–strain data of PyC pillars with $D = 4.6$–$12.7\,\mu m$. The micropillars deformed elastically up to ~20–30% strain, exhibiting marginal plastic strain (~8–10%) before failure. Dashed lines indicate the linear slopes. **b**, SEM images of a typical PyC micropillar described in **a**, before and after compression, which reveals the occurrence of brittle fracture via multiple fragments. **c**, Representative stress–strain dataset from the in situ deformation of a 2.25 μm diameter PyC pillar, which underwent significant plastic deformation up to 43.6% strain. Inset, SEM image of the micropillar before compression. **d**, A sequence of snapshots with numbered frames corresponding to the same-numbered red arrows in the stress–strain curve in **c**. **e**,**f**, SEM images of the compressed micropillar in **c** from front and back views. The nucleation and propagation of a splitting crack correspond to the strain burst indicated by the blue arrow in the stress–strain curve in **c**. **g**, Tensile stress–strain data of PyC dog-bone-shaped samples with gauge diameters of 0.7–2.0 μm. **h**, SEM images of a typical tensile specimen before and after the experiment. **i**, Statistical distribution of tensile fracture strengths.

it has ruptured into small pieces via brittle facture. To capture the in situ real-time deformation details of larger micropillars, we also performed in situ compressions on two micropillars with $D = 4.6$ and 7.1 μm (Supplementary Fig. 6), which indicates that catastrophic fracture occurred at the maximum applied stress.

We also carried out in situ compression experiments on micropillars with $D \lesssim 2$ μm. Figure 2c shows the compressive stress–strain response of a micropillar with diameter of 2.25 μm, which is characterized by a linear elastic regime up to ~10% strain, followed by an extensive plastic region up to ~25% strain, and a final stage in which the stress rapidly increased from 5.48 to 12.63 GPa with a strain increase of ~18%. This stress–strain curve is similar to that of rubber. After unloading from the maximum stress of 12.63 GPa, the micropillar partially recovered on release of ~10% elastic strain. Figure 2d depicts a sequence of snapshots of this sample during the experiment, with the numbered frames corresponding to the same numbered red arrows in Fig. 2c. We observed that the micropillar shortened and thickened gradually, without localization or catastrophic failure until the maximum applied strain of 43.6% (Supplementary Video 1). SEM images from front and back views of the pillar revealed a vertically aligned splitting microcrack (Fig. 2e,f), which probably nucleated under a large applied compressive stress, leading to a slight strain burst, indicated by the blue arrow in Fig. 2c. We defined the compressive strength of such samples to be the stress at the first burst. Supplementary Fig. 7 shows the detailed in situ deformation process of another micropillar with $D = 2.26$ μm under compression; this figure captures the nucleation and propagation of the splitting microcrack. The stress–strain data in Supplementary Fig. 7d show similar features to the plot in Fig. 2c. A clear difference between these two datasets is that a large strain burst is visible in Supplementary Fig. 7d, presumably caused by a burst of microcracks. Supplementary Fig. 8 shows the in situ compressive deformation of a typical 1.8 μm diameter micropillar, which contains an SEM image of a postmortem sample with a splitting microcrack that probably nucleated at a high stress of 13.7 GPa and led to a stress disturbance indicated by the orange arrow, which we define as the compressive strength of this sample. The residual carbon ring has marginal contribution to the strength (Supplementary Text 1 and Supplementary Fig. 9). Supplementary Figs. 10 and 11 summarize the compressive stress–strain data of all samples with $D = 1.8$–2.3 μm, all of which have similar features; the data indicate that samples with $D < 2.3$ μm can sustain large plastic deformation on compression. The SEM images in these figures indicate that all samples became tilted, and some formed microcracks, which implies that these samples failed due to the nucleation and propagation of microcracks under large strains. Nearly all stress–strain data in Supplementary Figs. 10 and 11 are characterized by nonlinear loading and unloading, indicating the presence of hysteresis in micropillars with $D < 2.3$ μm. We estimated such hysteresis to range from 3.67×10^8 to 5.21×10^9 J m^{-3}; its origin is discussed in Supplementary Text 2 and Supplementary Fig. 12.

We also conducted in situ uniaxial tension experiments on dog-bone-shaped PyC specimens. Figure 2g summarizes the tensile stress–strain data for samples with $D = 0.7$–2.0 μm. The average tensile strength of all 42 tested samples is 1.60 ± 0.55 GPa. We observed that all the samples failed via brittle fracture after linear elastic loading to an elongation of 10–25% (Supplementary Video 2). A typical smooth fracture surface is shown in Fig. 2h and Supplementary Video 2. A statistical distribution of the tensile strengths of all tested samples is shown in Fig. 2i and fits a two-parameter Weibull distribution:

$$f(\sigma_y) = \frac{m}{\sigma_0}\left(\frac{\sigma_y}{\sigma_0}\right)^{m-1} e^{-\left(\frac{\sigma_y}{\sigma_0}\right)^m} \quad (1)$$

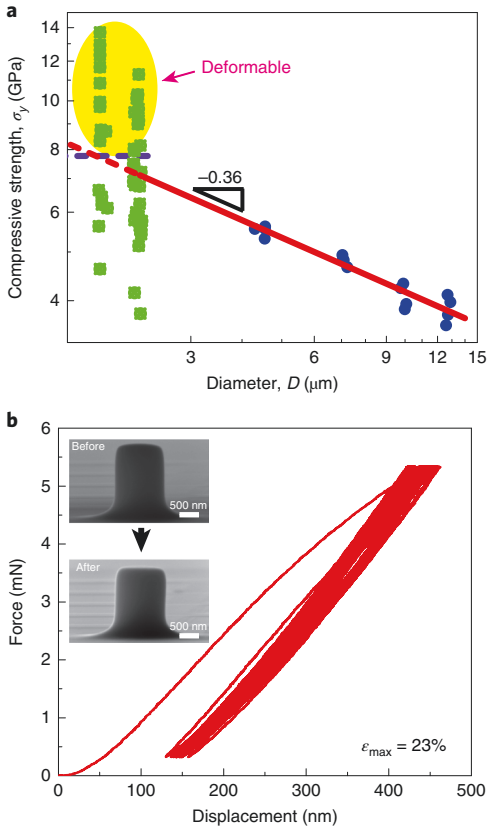

Fig. 3 | Change in strength with diameter and the ultra-large elastic limit of PyC micropillars. a, Variation in compressive strength with increasing micropillar diameter. Blue dashed line, average compressive strength of micropillars with $D < 2.3$ μm. **b**, Twenty-cycle force–displacement curve of a deformable pillar with $D = 1.28$ μm under a maximum compressive strain of ~23%, showing nearly full recovery in every cycle after the first cycle. The SEM images depict the pre-/post-deformation pillar from 20 loading cycles.

where σ_0 is a characteristic material strength and m is the Weibull modulus, which is a measure of the degree of strength dispersion and reflects the nature, severity and dispersion of internal flaws[31]. This distribution yields a characteristic strength σ_0 of 1.78 GPa and a low Weibull modulus m of 3.42, which indicates high variability in the failure strength. It suggests that the failure of PyC samples originates from internal flaws and the associated failure strength depends on the distribution of internal flaws and their sizes.

Figure 3a presents all experimental data obtained from the compression experiments and reveals, for samples with $D > 2.3$ μm, that the compressive strength σ_y increases with decreasing diameter D according to a power law, $\sigma_y \sim D^{-0.36}$. This scaling law agrees well with the theoretical prediction of $\sigma_y \sim D^{-0.40}$, which was derived from the asymptotic analysis of a fracture mechanics-based model[32] describing the compressive failure of quasi-brittle columns with characteristic diameter D. In this model, the columns were found to fail via the propagation of a splitting crack with an initial length h, similar to our experimental observations (Fig. 2f and Supplementary Fig. 7). The size effect on the strength of the samples originates from propagation of a splitting crack in a finite-sized column. Our microstructural analysis demonstrates that the PyC samples are composed of randomly distributed nanometre-sized curled graphene fragments, which inevitably create a matrix with a non-negligible fraction of defects. As the applied stress exceeds a critical value for crack initiation at some stress concentration sites, a

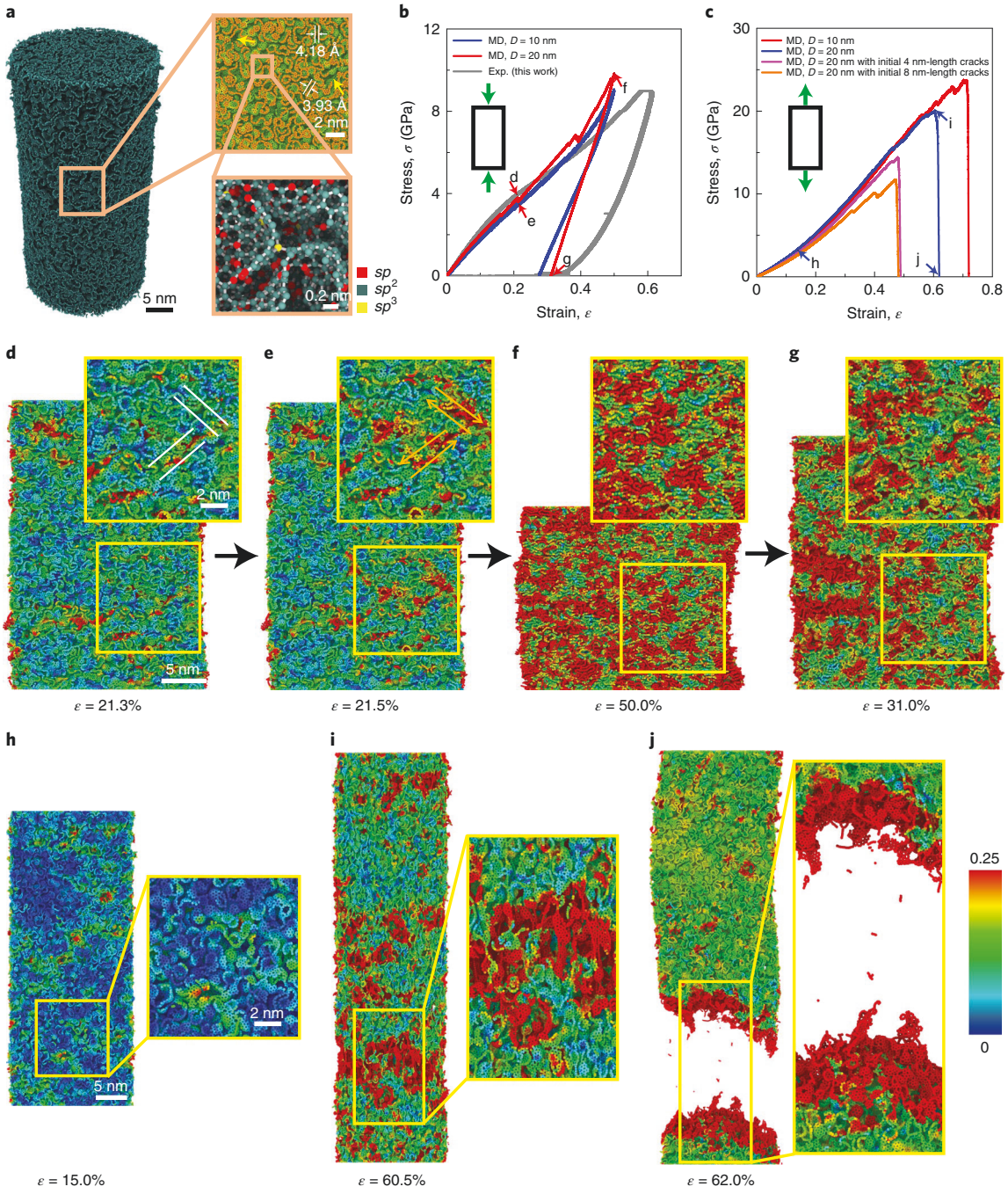

Fig. 4 | Atomistic simulations of the uniaxial compression and tension of PyC nanopillars. a, Atomic configurations and cross-sectional morphology of a simulated sample with $D = 20$ nm. **b**,**c**, Compressive (**b**) and tensile (**c**) stress–strain curves of PyC nanopillars. **d**–**g**, Snapshots of a deformed pillar at different compressive strains. **h**–**j**, Snapshots of a deformed pillar at different tensile strains. The atoms in **d**–**j** are coloured according to the von Mises atomic strain.

splitting crack can propagate via absorption and coalescence of voids/pores and/or other defects ahead of the crack tip. The theoretical model also offers an expression for the theoretical limit σ_{th} of the compressive strength[32]:

$$\sigma_{th} \approx 2.76\left(\frac{E^3\Gamma^2}{h^2}\right)^{1/5} \quad (2)$$

where E is Young's modulus and Γ is the fracture energy. Substituting the average experimental modulus of $E = 19.5$ GPa and $\Gamma = 29.9$ J m^{-2} (ref. [33]) into equation (2), we obtain $\sigma_{th} = 4.0$–13.5 GPa for the initial length of a splitting crack, $h = 100$ nm–1 μm. This predicted range is similar to the experimentally acquired compressive strengths of 3.8–13.7 GPa (Fig. 3a), which implies that the strength of PyC pillars with $D < 2.3$ μm approaches the theoretical limit. In the highlighted region in Fig. 3a, the micropillars can sustain an ultra-high compressive stress of 7.8–13.7 GPa and a high compressive strain in excess of 40%. Some detailed discussions about the compressive strength of the micropillars with $D < 2.3$ μm and tension–compression asymmetry are provided in Supplementary Text 3.

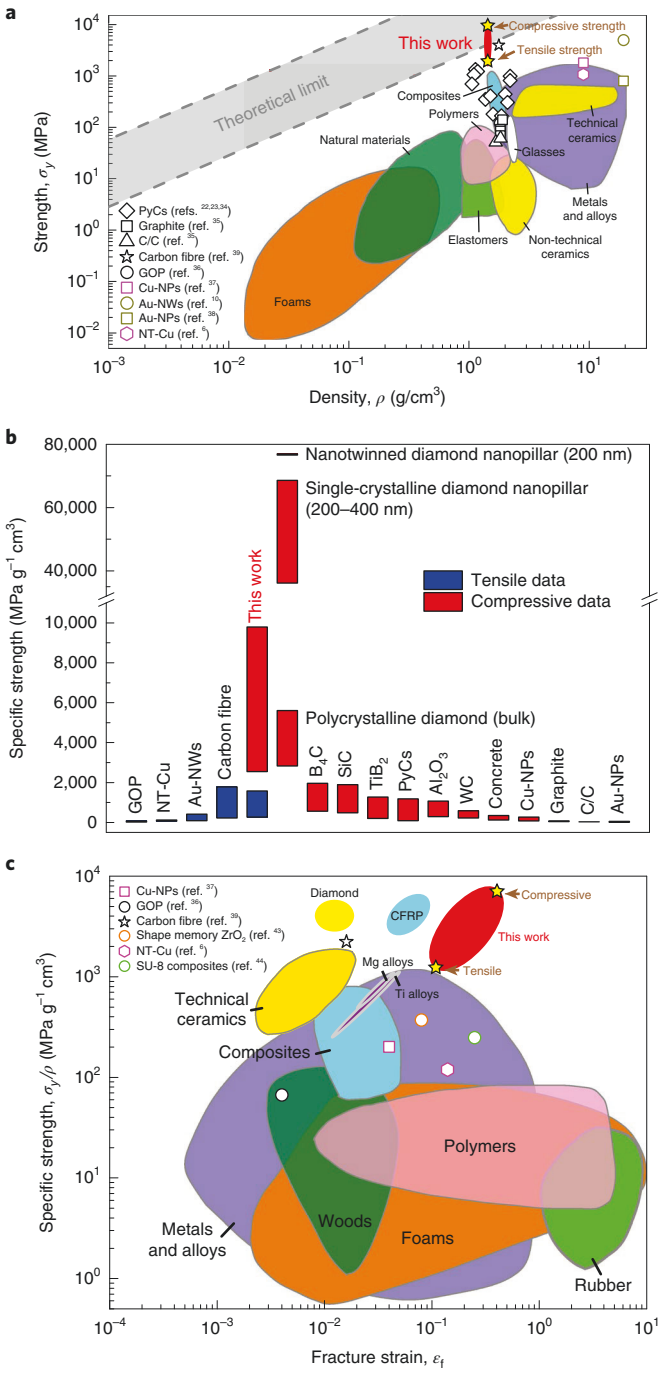

Fig. 5 | Summary of the combined ultra-high strength/specific strength and large deformability of PyC micropillars. a, Ashby chart of strength versus density for various structural materials, including the PyC micropillars in this work. **b**, Comparison of the specific tensile and compressive strengths of our PyC micropillars and other structural materials. **c**, Summary of specific strength versus fracture strain for our PyC micropillars and other structural materials. The excellent combination of specific strength and deformability of our PyC surpasses that of almost all other materials. Except for Cu-NPs, Au-NWs, Au-NPs and diamond nanopillars, the strength data of all other materials used for comparison in this figure are from measurements on bulk samples.

The compression and tension experiments revealed that PyC micropillars with $D < 2.3\,\mu m$ exhibit high deformability, that is, >40% compressive strain and ~20% tensile strain before failure. The cyclic compression experiments on these samples exhibited nearly full recovery after each cycle beyond the first one. Figure 3b shows a 20-cycle force–displacement dataset of a micropillar with $D = 1.28\,\mu m$ under a maximum compressive strain of 23%. These data, in combination with the pre-/post-deformation SEM images shown in the insets of Fig. 3b, indicate that after 20 cycles of compression to 23% strain, the micropillar recovered 95% of its original height. Such cyclic deformation and recovery are similar to those observed from nanoindentation[24,25] and compression[22,24,25] of PyC reported previously. A key difference is that previous studies[24,25] showed that, during compression, PyC samples undergo brittle fracture at a low fracture strain of ~3–6%. Our samples undergo cyclic deformation to a compressive strain as large as ~23% and nearly completely recover after cyclic loading (Fig. 3b).

Atomistic simulations of PyC nanopillars

We performed large-scale molecular dynamics (MD) simulations of the uniaxial compression and tension of PyC pillars with $D = 10$ and 20 nm and a constant aspect ratio of 2. Details of the simulations are presented in the Methods. The simulated samples consist of many ~1 nm sized curled graphene layer fragments and have a density of 1.4 g cm^{-3}, which is consistent with TEM observations of the experimental samples, as illustrated in Fig. 4a. These fragments were connected by covalent bonding or van der Waals interactions. The magnified image in Fig. 4a shows that the spacing between neighbouring graphene fragments is ~0.4 nm and that several sub-nanometre-sized voids are present adjacent to them, similar to the HRTEM images in Fig. 1d–f. The hybridization of carbon atoms in graphene is typically such that the *sp* bonds are mainly concentrated within the edges of the graphene layers, and the sp^3 bonds generally connect the neighbouring graphene layers to each other or form at their high-energy curved surfaces (Fig. 4a). In the simulated samples, the fraction of sp^2 bonds is at least one order of magnitude higher than the fractions of *sp* and sp^3 bonds (Supplementary Fig. 13), indicating the dominance of the sp^2 bonds, which is consistent with the EELS analyses (Fig. 1g). Figure 4b,c presents the compressive and tensile stress–strain curves from the MD simulations, which show similar trends and stresses to the experimental data, indicating similar microstructures and densities of the simulation and experimental samples. Figure 4d–g presents several snapshots of the cross-section of a simulated sample at different compressive strains. In the initial elastic stage, the curled graphene layers approach each other, and some are bent significantly (Fig. 4d). As the applied compressive strain increases, several graphene layers slip relative to the neighbouring ones, leading to abrupt fracture of the graphene layers under shear (Fig. 4d,e). Such discrete failure events give rise to stress fluctuations at a strain of 21.5% (Fig. 4b). At a compressive strain of 50%, the sub-nanometre-sized voids collapse and cause densification of nanopillars. Slight tilting occurs due to the interlayer slipping and shear of neighbouring graphene layers (Fig. 4f). During unloading, the nanopillar exhibits a recovery associated with the release of stored elastic strain energy; the distances between graphene layers increase, and the sub-nanometre-sized voids partially reopen (Fig. 4g). During both loading and unloading, we observe rearrangement of graphene fragments and interlayer shear/friction between neighbouring graphene layers (Fig. 4d–g), which might have contributed to the observed hysteresis and associated energy dissipation in smaller pillars (Supplementary Text 2). The recovered strain is 19%, which is comparable to the experimental results (Fig. 4b). More deformation details are provided in Supplementary Video 3.

Another similarity to the experiments is that all simulated nanopillars subjected to tension failed after undergoing nearly linear elastic deformation (Fig. 4c). Figure 4h–j shows a sequence of snapshots of the cross-section of a stretched sample at different strains. We observed that a number of nanoscale cavities have nucleated,

expanded under tension and then coalesced, leading to the formation of nanoscale cracks (Fig. 4i and Supplementary Fig. 14a). Eventually, these nanoscale cracks propagate in the direction normal to the tensile loading, resulting in a smooth fracture surface (Fig. 4j and Supplementary Fig. 14b). This cleavage fracture is similar to the experimental observations in Fig. 2h. More details of the nanopillar under tension are presented in Supplementary Video 4. The tensile strength decreases from 20 GPa to ~12 GPa after introducing cracks into the nanopillar, which indicates that the presence of initial flaws/imperfections facilitates a significant reduction in the tensile strength (Supplementary Text 4 and Supplementary Fig. 15).

Mechanical properties

Figure 5a plots a strength-versus-density landscape for PyC micropillars and various structural materials, including conventional structural materials[4,22,23,34] and recently reported high-strength nanomaterials[6,10,35–38]. This plot reveals that the strength of the PyC micropillars is ~1–3 orders of magnitude higher than those of most structural materials, including bulk PyCs[22,23,34], graphite[35], carbon fibre-reinforced carbon (C/C)[35], graphene oxide paper (GOP)[36], copper nanopillars (Cu-NPs)[37], gold nanopillars (Au-NPs)[38] and bulk nanotwinned copper (NT-Cu)[6], and falls within the theoretical limit region for the uniaxial strength of structural materials proposed in ref. [26]. The strength of the PyC micropillars is comparable to those of carbon microfibres[39] and gold nanowires (Au-NWs)[10], but its density is ~79% and 7.3% those of carbon fibres and Au-NWs, respectively. As indicated in Supplementary Fig. 16, the PyC micropillars exhibit a superior combination of high strength and high deformability, allowing them to overcome the classical trade-off between strength and deformability that has plagued all materials so far. It appears that the PyC micropillars possess maximum tensile and compressive strengths of 2.5 GPa and 13.7 GPa and a low density of 1.4 g cm^{-3}, thereby also overcoming the conflict between high strength and low density, leading to an ultra-high specific strength of 9.79 GPa cm^3 g^{-1}. Figure 5b shows the specific tensile and compressive strengths of various materials and reveals that the PyC micropillars have at least one order of magnitude greater specific strength than for GOP[36], NT-Cu[6] and Au-NWs[10], and comparable to that of carbon microfibres[39]. Their specific compressive strengths exceed those of polycrystalline diamond (which has the highest specific compressive strength in all bulk materials so far[26]), common hard ceramics[40] (such as B_4C, SiC and Al_2O_3), metallic nanopillars (Cu-NPs[37] and Au-NPs[38]) and carbon materials (PyCs[22,23,34], graphite and C/C[35]), but are lower than the highest specific compressive strength reported for single-crystalline and nanotwinned diamond nanopillars[41,42]. Figure 5c shows an Ashby plot of specific strength versus fracture strain for our PyC and various other materials, including shape memory zirconia[43], SU-8 composites[44], titanium alloys, magnesium alloys, carbon fibre reinforced polymer (CFRP) and polycrystalline diamond. Notably, our PyC occupies a hitherto unexplored space in the Ashby diagram, where no other materials reach. The PyC micropillars exhibit 1.5–8.2 times higher compressive strength and at least one order of magnitude larger fracture strain than existing PyC[23,25], which is attributed to differences in the microstructures and sample sizes of these materials (Supplementary Text 5).

Conclusions

We synthesized the PyC micropillars with diameters of 0.7–12.7 μm via DLW and pyrolysis, to obtain a microstructure consisting of ~1.0–1.5 nm curled graphene fragments. Compressive and tensile experiments showed that these micropillars exhibit an exceptional combination of substantial deformability and ultra-high elastic limit, strength and specific strength. Large-scale MD simulations revealed detailed deformation mechanisms in the PyC pillars; that is, compressive deformation was dominated by densification of the structure and slipping/shear of the graphene layers, while tensile deformation was governed by the extension of initial flaws or by the nucleation, growth and coalescence of nanoscale cavities. These deformation mechanisms are responsible for the unique combination of desirable properties including high deformability, high elastic limit and high strength. Our findings demonstrate critical connections between the microstructure, deformation mechanisms and mechanical properties of PyC materials, and provide potential routes for designing and synthesizing new high-performance carbon materials.

Online content

Any methods, additional references, Nature Research reporting summaries, source data, statements of code and data availability and associated accession codes are available at https://doi.org/10.1038/s41565-019-0486-y.

Received: 11 May 2018; Accepted: 24 May 2019;
Published online: 8 July 2019

References

1. Meyers, M. A. & Chawla, K. K. *Mechanical Behavior of Materials* (Cambridge Univ. Press, 2009).
2. Ashby, M. F. in *Materials Selection in Mechanical Design* 4th edn, Ch. 4, 57–96 (Butterworth-Heinemann, 2011).
3. Muth, J. T., Dixon, P. G., Woish, L., Gibson, L. J. & Lewis, J. A. Architected cellular ceramics with tailored stiffness via direct foam writing. *Proc. Natl Acad. Sci. USA* **114**, 1832–1837 (2017).
4. Lucas, R., Meza, L. R., Das, S. & Greer, J. R. Strong, lightweight and recoverable three-dimensional ceramic nanolattices. *Science* **345**, 1322–1326 (2014).
5. Wang, H. et al. Ultralight, scalable and high-temperature-resilient ceramic nanofiber sponges. *Sci. Adv.* **3**, e1603170 (2017).
6. Lu, L., Shen, Y., Chen, X., Qian, L. & Lu, K. Ultrahigh strength and high electrical conductivity in copper. *Science* **304**, 422–426 (2004).
7. Sanders, P. G., Eastman, J. A. & Weertman, J. R. Elastic and tensile behavior of nanocrystalline copper and palladium. *Acta Mater.* **45**, 4019–4025 (1997).
8. Zhang, Y. et al. Microstructures and properties of high-entropy alloys. *Prog. Mater. Sci.* **61**, 1–93 (2014).
9. Greer, J. R. & Hosson, J. T. Plasticity in small-sized metallic systems: intrinsic versus extrinsic size effect. *Prog. Mater. Sci.* **56**, 654–724 (2011).
10. Wu, B., Heidelberg, A. & Boland, J. J. Mechanical properties of ultrahigh-strength gold nanowires. *Nat. Mater.* **4**, 525–529 (2005).
11. Lowry, M. B. et al. Achieving the ideal strength in annealed molybdenum nanopillars. *Acta Mater.* **58**, 5160–5167 (2010).
12. Gogotsi, Y. Not just graphene: the wonderful world of carbon and related nanomaterials. *MRS Bull.* **40**, 1110–1121 (2015).
13. Lee, C., Wei, X., Kysar, J. W. & Hone, J. Measurement of the elastic properties and intrinsic strength of monolayer graphene. *Science* **321**, 385–388 (2008).
14. Rasool, H. I., Ophus, C., Klug, W. S., Zettl, A. & Gimzewski, J. K. Measurement of the intrinsic strength of crystalline and polycrystalline graphene. *Nat. Commun.* **4**, 2811 (2013).
15. Zhang, P. et al. Fracture toughness of graphene. *Nat. Commun.* **5**, 3782 (2014).
16. Wei, Y. et al. The nature of strength enhancement and weakening by pentagon–heptagon defects in graphene. *Nat. Mater.* **11**, 759–763 (2012).
17. Song, Z., Artyukhov, V. I., Wu, J., Yakobson, B. I. & Xu, Z. Defect-detriment to graphene strength is concealed by local probe: the topological and geometrical effects. *ACS Nano* **9**, 401–408 (2015).
18. Cao, A., Dickrell, P. L., Sawyer, W. G., Ghasemi-Nejhad, M. N. & Ajayan, P. M. Super-compressible foam-like carbon nanotube films. *Science* **310**, 1307–1310 (2005).
19. Qu, L., Dai, L., Stone, M., Xia, Z. & Wang, Z. L. Carbon nanotube arrays with strong shear binding-on and easy normal lifting-off. *Science* **322**, 238–242 (2008).
20. Barg, S. et al. Mesoscale assembly of chemically modified graphene into complex cellular networks. *Nat. Commun.* **5**, 4328 (2014).
21. Qin, Z., Jung, G. S., Kang, M. J. & Buehler, M. J. The mechanics and design of a lightweight three-dimensional graphene assembly. *Sci. Adv.* **3**, e1601536 (2017).
22. Zhang, H., Lopez-Honorato, E. & Xiao, P. Fluidized bed chemical vapor deposition of pyrolytic carbon-III. Relationship between microstructure and mechanical properties. *Carbon* **91**, 346–357 (2015).
23. Stein, I. Y. et al. Structure–mechanical property relations of non-graphitizing pyrolytic carbon synthesized at low temperatures. *Carbon* **117**, 411–420 (2017).

24. Zhao, Z. et al. Nanoarchitectured materials composed of fullerene-like spheroids and disordered graphene layers with tunable mechanical properties. *Nat. Commun.* **6**, 6212 (2015).
25. Hu, M. et al. Compressed glassy carbon: an ultrastrong and elastic interpenetrating graphene network. *Sci. Adv.* **3**, e1603213 (2017).
26. Bauer, J., Schroer, A., Schwaiger, R. & Kraft, O. Approaching theoretical strength in glassy carbon nanolattices. *Nat. Mater.* **15**, 438–443 (2016).
27. Li, X. & Gao, H. Mechanical metamaterials: smaller and stronger. *Nat. Mater.* **15**, 373–374 (2016).
28. Harris, P. J. New perspectives on the structure of graphitic carbons. *Crit. Rev. Solid State* **30**, 235–253 (2005).
29. Cançado, G. L. et al. General equation for the determination of the crystallite size of nanographite by Raman spectroscopy. *Appl. Phys. Lett.* **88**, 163106 (2006).
30. Bruley, J., Williams, D. B., Cuomo, J. J. & Pappas, D. P. Quantitative near-edge structure analysis of diamond-like carbon in the electron microscope using a two-window method. *J. Microsc.* **180**, 22–32 (1995).
31. Basu, B., Tiwari, D., Kundu, D. & Prasad, R. Is Weibull distribution the most appropriate statistical strength distribution for brittle materials? *Ceram. Int.* **35**, 237–246 (2009).
32. Bazant, Z. P. & Xiang, Y. Size effect in compression fracture: splitting crack band propagation. *J. Eng. Mech.* **13**, 162–172 (1997).
33. Zhao, J. X., Bradt, R. C. & Walker, P. L. The fracture toughness of glassy carbons at elevated temperatures. *Carbon* **23**, 15–18 (1985).
34. Yajima, S., Hirai, T. & Hayase, T. Micro-hardness of pyrolytic graphite and siliconated pyrolytic graphite. *Tanso* **69**, 41–47 (1972).
35. Oku, T., Kurumada, A., Imamura, Y. & Ishihara, M. Effects of ion irradiation on the hardness properties of graphites and C/C composites by indentation tests. *J. Nucl. Mater.* **381**, 92–97 (2008).
36. Dikin, D. et al. Preparation and characterization of graphene oxide paper. *Nature* **448**, 457–460 (2007).
37. Jang, D., Li, X., Gao, H. & Greer, J. R. Deformation mechanisms in nanotwinned metal nanopillars. *Nat. Nanotechnol.* **7**, 594–601 (2012).
38. Greer, J. R., Oliver, W. C. & Nix, W. D. Size dependence of mechanical properties of gold at the micron scale in the absence of strain gradients. *Acta Mater.* **53**, 1821–1830 (2005).
39. Fu, S. Y., Lauke, B., Mäder, E., Yue, C. Y. & Hu, X. Tensile properties of short-glass-fiber- and short-carbon-fiber-reinforced polypropylene composites. *Compos. Part A* **31**, 1117–1125 (2000).
40. Dunlay, W. A., Tracy, C. A. & Perrone, P. J. *A Proposed Uniaxial Compression Test for High Strength Ceramics* (US Army, 1989).
41. Wheeler, J. M. et al. Approaching the limits of strength: measuring the uniaxial compressive strength of diamond at small scales. *Nano Lett.* **16**, 812–816 (2016).
42. Xu, B. & Tian, Y. High pressure synthesis of nanotwinned ultrahard materials. *Acta Phys. Sin.* **66**, 036201 (2017).
43. Lai, A., Du, Z., Gan, C. L. & Schuh, C. A. Shape memory and superelastic ceramics at small scales. *Science* **341**, 1505–1508 (2013).
44. Dusoe, K. J. et al. Ultrahigh elastic strain energy storage in metal-oxide-infiltrated patterned hybrid polymer nanocomposites. *Nano Lett.* **17**, 7416–7423 (2017).

Acknowledgements

X.L. acknowledges financial support from the National Natural Science Foundation of China (grants 11522218 and 11720101002) and the National Basic Research of China (grant 2015CB932500). H.G. acknowledges funding from the National Science Foundation (grant DMR-1709318). J.R.G. acknowledges financial support by the US Department of Energy, Office of Basic Energy Sciences (DOE-BES) under grant DE-SC0006599. A.V. acknowledges the financial support of the Resnick Sustainability Institute at Caltech. The authors thank G. R. Rossman for assistance with Raman spectroscopy measurements, J. Yao for help with SIMS measurements and K. Narita for assistance with density measurements of pyrolytic carbon.

Author contributions

X.Z., X.L., H.G. and J.R.G. conceived and designed the experiments and modelling. X.Z. and A.M. synthesized the experimental samples. X.Z. performed the in situ and ex situ compression experiments. A.M. performed the in situ tension experiments. A.K. and X.Z. performed the HRTEM and EELS analyses. A.V. and L.Z. performed the Raman spectroscopy measurements. L.Z. conducted the atomistic simulations. X.Z., L.Z. and X.L. developed the model. X.Z., L.Z., X.L., H.G. and J.R.G. wrote the manuscript. All authors analysed the data, discussed the results and commented on the manuscript.

Competing interests

The authors declare no competing interests.

Additional information

Supplementary information is available for this paper at https://doi.org/10.1038/s41565-019-0486-y.

Reprints and permissions information is available at www.nature.com/reprints.

Correspondence and requests for materials should be addressed to H.G., J.R.G. or X.L.

Peer review information: *Nature Nanotechnology* thanks Maria Pantano, Ping Xiao and other anonymous reviewer(s) for their contribution to the peer review of this work.

Publisher's note: Springer Nature remains neutral with regard to jurisdictional claims in published maps and institutional affiliations.

Methods

Fabrication of samples. The fabrication process for the PyC micropillars comprised two steps: two-photon lithography and high-temperature pyrolysis. We first synthesized the pillars using 3D TPL DLW (Photonic Professional, Nanoscribe) with the dip-in laser lithography configuration, a ×63 objective and commercial IP-Dip photoresist. For pyrolysis, the printed polymeric samples were heated to 900 °C at a ramp rate of 7.5 °C min^{-1} in a vacuum tube furnace, then maintained at the target temperature for 5 h and finally cooled to room temperature at a natural rate. After pyrolysis, the pillar dimensions shrank to ~20–25% of their original values, corresponding to 98% volumetric contraction. The diameter of the PyC pillars for the compression experiments varied from 1.28 to 12.7 µm. Dog-bone-shaped samples with gauge sections of 0.7–2.0 µm were synthesized using the same procedure as used for the tensile experiments. For the compressive tests, the initial polymer samples were cylindrical and had a constant aspect ratio of ~2.0. After pyrolysis, the samples underwent nearly uniform shrinkage in all dimensions, forming a residual carbon ring on the constraining silicon substrate. Excluding the height of the carbon ring, the cylinders had an aspect ratio of 1.4–1.8 according to SEM observations. For the tensile tests, the initial dog-bone-shaped polymer samples had a constant height of ~15 µm with different diameters in the gauge sections. After pyrolysis, the overall height of all tensile samples shrank to ~3 µm, and the diameter in the gauge sections varied from 0.7 to 2.0 µm, which indicates the aspect ratio is in the range from 4.3 to 1.5.

Microstructural characterization. The microstructure of the PyC micropillars was characterized by an FEI Technai TF-30 TEM at an accelerating voltage of 300 kV. The samples for TEM analyses were prepared using a site-specific lift-out technique. Samples with thickness of ~1 µm were first carved from the PyC micropillars via FIB milling (Helios Nanolab 600i). These samples were then attached to the TEM grid using I-beam (or e-beam) deposited organometallic Pt glue and thinned to ~50–60 nm via FIB milling. The milling was carried out using progressively lower voltages and currents: 20 kV and 0.6 nA, 5 kV and 27 pA, and 5 kV and 10 pA for the final polish. To minimize/reduce the FIB-induced damage on the TEM samples[45], we polished the samples by repeating 2 min low-energy FIB milling five times on both sides of the samples at a voltage of 5 kV and a current of 10 pA, which has been shown to minimize FIB-induced damage for various materials[46,47]. EELS analysis was conducted in an FEI Technai TF-20 at an accelerating voltage of 200 kV to estimate the relative fractions of sp^2 and sp^3 bonds. For each TEM sample, we collected six EELS spectra at different sites within the sample. Raman spectra were collected at room temperature using a Raman spectrometer (Renishaw M1000 Micro).

Nanomechanical experiments. Uniaxial compression on samples with diameters of 1.28–2.28 µm and all uniaxial tension experiments were conducted at a constant nominal strain rate of 10^{-3} s^{-1} in a custom-made in situ nanomechanical instrument (SEMentor)[48] with a 10-µm-diameter flat punch indenter tip and a tensile grip, respectively. The SEMentor allowed precise control of deformation with simultaneous video capture[48]. Samples with larger diameters of 4.6–12.7 µm were compressed in a nanoindenter (Nanoindenter G200 XP, Agilent/Keysight Technologies) with a 120-µm-diameter flat punch at a constant loading rate of 0.02–0.2 mN s^{-1} because of the load limit in the in situ instrument. Additional compression experiments were conducted on samples with diameters of 2.21–12.7 µm in the G200 to independently validate the results of the in situ experiments. We also compressed two micropillars with diameters of 4.6 and 7.1 µm in an in situ SEM instrument (PI-88, Hysitron) with high-loading sensors to capture in situ real-time deformation details of larger micropillars.

Estimation of the density of PyC micropillars from TEM analysis. HRTEM images revealed that the PyC micropillars consist of nanometre-sized, randomly distributed curved graphene layers. Supplementary Fig. 3 provides a comprehensive set of images that pertain to the estimation of density in these materials. Supplementary Fig. 3a illustrates the distribution of the curved graphene segments, and Supplementary Fig. 3b shows an individual representative graphene segment, where the average end-to-end length is L and the spacing between neighbouring layers is L_s. We built on an existing geometric model[23] to estimate the density (ρ_{PC}) of the PyC. The density of the curved graphene layers, ρ_{CGL}, can be expressed as

$$\rho_{CGL} = \frac{\beta L_G}{L_S}\rho_G \tag{3}$$

where ρ_G is the density of single-crystalline graphite ($\rho_G = 2.25$ g cm^{-3}), L_G is the interlayer distance in single-crystalline graphite ($L_G = 0.34$ nm) and β is a shape factor that reflects the curvature of the curved graphene layer, where $\beta = 1$ represents a flat graphene layer and $\beta = \pi/2$ corresponds to a semicircle. Supplementary Fig. 3c shows a schematic of a stacking structure of two curved graphene layers. Using this geometry as a guide, the density of PyC can be estimated as[23]

$$\rho_{PC} = \rho_{CGL}\left(\frac{1}{1 + 0.5(L/L_S)\sin\theta\cos\theta}\right) \tag{4}$$

where θ is the orientation angle between two graphene layers in a typical unit cell (Supplementary Fig. 3c) and $\theta = 45°$ corresponds to isotropic PyC[23], where the curved graphene layers are randomly distributed. Based on TEM observations (Fig. 1e,f), we obtained $\beta = 1$ or $\pi/2$, $\theta = \pi/4$, $L_s = 0.4$ nm and $L = 1.0$–1.5 nm. Because HRTEM observations have higher accuracy than the approximate prediction based on Raman spectra, here we took the characteristic crystallite size L of the curled carbon layer to be 1.0–1.5 nm, as derived from HRTEM observations. By substituting these parameters into equations (3) and (4), we obtain $\rho_{PC} = 1.0$–1.8 g cm^{-3}. Supplementary Fig. 3d compares our modified model, a previous geometrical model and experimental data on bulk PyC. The predictions from our modified model show reasonable agreement with experimental data[22,34].

To reliably measure the density of PyC, we used a different 3D printing process—digital light processing (Ember)—to print circular plates with diameters of 18 mm, which were then pyrolysed under the same conditions as the TPL-produced PyC micropillars. After pyrolysis, we measured the mass and dimension of PyC plates using an analytical balance and optical microscopy to estimate their densities in the range of 1.4–1.6 g cm^{-3}. We further constructed full atomic configurations of five 10-nm-diameter nanopillars with densities varying from 1.0 to 1.8 g cm^{-3} (Supplementary Fig. 17) and performed additional atomistic simulations to mimic their uniaxial compression. Supplementary Fig. 18 shows the simulated stress–strain curves of these five nanopillars, together with a typical experimental stress–strain dataset. This plot reveals that only nanopillars with a density of 1.4 g cm^{-3} have the same modulus and very similar stress–strain response to experimental data. The combination of these experimental measurements and atomistic simulations unambiguously points to a density of PyC pillars of ~1.4 g cm^{-3}.

Estimation of carbon fragment size based on Raman spectra. Raman spectroscopy is widely used to investigate defects and disorder in carbon nanomaterials, including graphene, carbon nanotubes and glassy carbon[29,49]. The ratio of the integrated area under the D peak and that under the G peak, I_D/I_G, in a Raman spectrum is related to the in-plane crystallite size (L) of carbon materials by the following equation[29]:

$$L \approx \alpha\lambda_l^4\left(\frac{I_D}{I_G}\right)^{-1} \tag{5}$$

where α is a constant of 2.4×10^{-10} and λ_l is the wavelength (in units of nanometres) of laser used in the Raman experiment. We first fitted the Raman spectra of a PyC micropillar using four Lorentzian-shaped bands (G, D_1, D_2, D_4) at the Raman shifts of ~1,580, 1,350, 1,620 and 1,200 cm^{-1} and a Gaussian-shaped band (D_3) at 1,500 cm^{-1} in ref. [49]. Supplementary Fig. 19 contains three typical Raman spectra with examples of fitting procedure for different bands. After obtaining the fitted bands, we calculated I_D and I_G by integrating the areas under the D and G bands with shift from 800 to 2,000 cm^{-1} (ref. [49]). Based on all the Raman spectra measured on micropillars with diameters of 1.0–12.7 µm (Supplementary Fig. 4), we evaluated the average size of graphene layer fragment L as 1.7–2.5 nm using equation (5) (Supplementary Table 1). This result is in agreement with the characteristic size of 1.0–1.5 nm of curved graphene layers estimated based on HRTEM analysis.

Estimation of the fraction of sp^2 bonds based on EELS. EELS spectra provide quantitative information about the electronic structure of carbon materials[25,30]. We used the common two-window method[30] to estimate the fraction of sp^2 bonds in the PyC micropillars and used the EELS data of raw glassy carbon, which is fully sp^2-hybridized, as reference. From the EELS data of PyC (in Fig. 1g and Supplementary Fig. 5) and raw glassy carbon, we calculated the areas under the two windows around the π^* and σ^* peaks (denoted I_π and I_σ) of both materials. A normalized ratio N_{int} can then be calculated as[25,30]

$$N_{int} = \frac{I_\pi^{PC}/I_\sigma^{PC}}{I_\pi^{RG}/I_\sigma^{RG}} \tag{6}$$

where the superscripts 'PC' and 'RG' represent PyC and raw glassy carbon, respectively. The normalized ratio N_{int} is also a function of the fraction of sp^2 bonds f as follows[25,30]:

$$N_{int} = \frac{3f}{4-f} \tag{7}$$

Setting equations (6) and (7) equal to each other, we calculated the fraction of sp^2 bonds in the PyC micropillars to be 94.4 ± 3.2% based on all the EELS data shown in Fig. 1g and Supplementary Fig. 5.

Atomistic simulations. We performed a series of large-scale atomistic simulations that emulate the uniaxial compression and tension of PyC nanopillars using LAMMPS[50]. We used the adaptive intermolecular reactive empirical bond order force field[51] in all simulations to describe the interatomic interactions. This

force field describes the bonded interactions based on bond order, non-bonded interactions (that is, van der Waals) and torsional interactions, which enables it to capture the formation and breakage of carbon bonds[51]. We first constructed the simulated samples using the microstructure determined experimentally from the HRTEM images, which contained many curved graphene fragments with an average size of 1 nm. These graphene fragments were extracted from C_{84} fullerene. A large number of such graphene fragments with random orientations were initially hexagonally close-packed in a simulation box with dimensions of $27.5\times27.2\times54.3\,nm^3$. This system was then equilibrated by energy minimization and then relaxation at 300 K for 50 ps under an isothermal–isobaric (NPT) ensemble. After equilibration, the simulated system was hydrostatically compressed at a constant strain rate of $10^9\,s^{-1}$ at 300 K for 550 ps via a canonical (NVT) ensemble until the density of the simulated sample condensed to $1.40\,g\,cm^{-3}$. After compression, the hydrostatic pressure increased to 10 GPa. We then performed a melting-and-quenching process while holding the volume constant by confining all the dimensions of the simulation box. During this process, we first increased the temperature from 300 K to 1,200 K within 50 ps, then held the temperature at 1,200 K for 300 ps to fuse the graphene flakes, and finally reduced the temperature from 1,200 K to 300 K in 50 ps. Such a high-temperature and high-pressure process is used to facilitate/accelerate the fusion of graphene flakes. We then relaxed the simulated sample at 300 K for 200 ps under an NPT ensemble to relieve the pressure to zero. After relaxation, the simulated sample had dimensions of $20.5\times20.4\times40.8\,nm^3$ and a density of $\sim1.40\,g\,cm^{-3}$. Throughout these processes, periodic boundary conditions were imposed in all three directions of the simulated samples.

We then extracted nanopillars with diameters of 10 and 20 nm from the above relaxed cubic sample to perform uniaxial deformation simulations. We maintained the aspect ratios of all simulated nanopillars near 2 to mimic experiments. After equilibration, we compressed or stretched the nanopillars along the axial direction at a constant strain rate of $5\times10^8\,s^{-1}$ and a constant temperature of 300 K via an NVT ensemble. During simulations, the stress of each atom was calculated based on the Virial stress theorem. Axial compressive or tensile stresses were obtained by averaging over all atoms in the nanopillars.

We also investigated the influence of flaws, such as nanoscale cracks, on the tensile response of simulated samples. We introduced a few nanoscale cracks with lengths of 4 or 8 nm by removing some atoms from the 'as-constructed' samples. After equilibration, we applied the same tensile loading to the samples with nanocracks as to the 'as-constructed' ones and compared their stress–strain response and fracture. Throughout the simulations, periodic boundary conditions were imposed along the axial direction of the simulated nanopillars. We identified the sp, sp^2 and sp^3 bonds of the simulated samples by counting the coordination number of each atom. We found that the sp bonds were mainly distributed at the edges of the curved graphene layers, and the sp^3 bonds either connected the neighbouring graphene layers to each other or were formed at some high-energy curved surfaces of the graphene layers. The fractions of sp, sp^2 and sp^3 hybridized bonds in the 'as-constructed' samples were 8.8%, 89.1% and 1.8%, respectively, indicating that sp^2 bonding was dominant in the simulated samples; this was consistent with our experimental results (Fig. 1g). The remaining 0.3% of bonds were dangling bonds. This fraction of sp^2 bonds is close to that based on EELS measurement, $94.4\pm3.2\%$, and the relative fraction of sp bonds is one order magnitude lower than that of sp^2 bonds. Existing studies have investigated the microstructure of amorphous carbon (that is, glassy carbon) with different densities using density functional theory (DFT)[52], showing that the emergence of sp bonding for amorphous carbon with densities below $2.0\,g\,cm^{-3}$ is caused by loose atomic arrangements within the material[52]. The microstructure (especially bonding structure) of our simulated sample is very similar to that of the amorphous carbon predicted by the DFT simulations.

Elemental analysis. The micrometre-sized dimensions of PyC samples mean it is challenging to measure their elemental compositions directly using an elemental analyser. We used SIMS (TOF-SIMS 5, GmbH-Muenster) with a pulsed 30 keV Bi^+ primary ion source and a current of 1.0 pA to remove the ~10 nm outer surface and to then carry out the elemental analysis on our PyC samples. We also extracted millimetre-sized samples of commercial glassy carbon (TOKAI Carbon) to use as a reference material and measured the intensities of secondary ions using the same method. For the SIMS analysis, we measured six PyC micropillars and three glassy carbon samples. Supplementary Fig. 20a,b summarizes all the SIMS spectra, and shows that both materials contain predominantly carbon and traces of oxygen and hydrogen. We integrated the areas under the characteristic oxygen and hydrogen peaks in the SIMS spectra (Supplementary Fig. 20a,b), and normalized them with that of the carbon peak; we thus found the relative contents of oxygen and hydrogen to be only a fraction (0.52 for oxygen and 0.88 for hydrogen) of those in the commercial glassy carbon. Elemental composition using a CE-440 elemental analyser (Exeter Analytical) revealed that the mass fraction of carbon in the commercial glassy carbon is ≥96.8%, that of oxygen is ~3.1% and that of hydrogen is <0.1%. These numbers probably overestimate the actual oxygen content because of the greater concentration of oxygen absorbed onto sample surfaces. Combining the relative contents of oxygen and hydrogen from SIMS analysis, we estimated the mass fractions of each element in the PyC samples in this work to be 98.2% carbon, 1.7% oxygen and <0.1% hydrogen, which confirms the dominance of carbon within the pyrolysed samples. Trace amounts of oxygen and hydrogen are not expected to have a significant influence on the mechanical properties of the material.

Data availability

The data that support the plots and other findings of this study are available from the corresponding authors upon request.

References

45. Mayer, J., Giannuzzi, L. A., Kamino, T. & Michael, J. TEM sample preparation and FIB-induced damage. *MRS Bull.* **32**, 400–407 (2007).
46. Ke, X. et al. TEM sample preparation by FIB for carbon nanotube interconnects. *Ultramicroscopy* **109**, 1353–1359 (2009).
47. Schaffer, M., Schaffer, B. & Ramasse, Q. Sample preparation for atomic-resolution STEM at low voltages by FIB. *Ultramicroscopy* **114**, 62–71 (2012).
48. Jennings, A. T. & Greer, J. R. Tensile deformation of electroplated copper nanopillars. *Philos. Mag.* **91**, 1108–1120 (2011).
49. Sadezky, A., Muckenhuber, H., Grothe, H., Niessner, R. & Pöschl, U. Raman microspectroscopy of soot and related carbonaceous materials: spectral analysis and structural information. *Carbon* **43**, 1731–1742 (2005).
50. Plimpton, S. Fast parallel algorithms for short-range molecular dynamics. *J. Comp. Phys.* **117**, 1–19 (1995).
51. Stuart, S. J., Tutein, A. B. & Harrison, J. A. A reactive potential for hydrocarbons with intermolecular interactions. *J. Chem. Phys.* **112**, 6472–6486 (2000).
52. Deringer, V. L. & Csanyi, G. Machine learning based interatomic potential for amorphous carbon. *Phys. Rev. B* **95**, 094203 (2017).